A 2D BEAM-COLUMN JOINT MACRO-ELEMENT FOR THE NON-LINEAR ANALYSIS OF RC FRAMES

Bartolomeo Pantò[1], Salvatore Caddemi[2], Ivo Caliò[2], Enrico Spacone[3]

[1]Department of Civil and Environmental Engineering, Imperial College London, South Kensington Campus, London SW7 2AZ, United Kingdom.

[2] Department of Engineering and Architecture, University of Catania, Viale Andrea Doria 6, 95125 Catania, Italy.

[3] University G. d'Annunzio of Chieti - Pescara, Department of Engineering and Geology, Viale Pindaro 42, 65127 Pescara, Italy.

Recent earthquakes have shown that the seismic behavior of non-code-conforming reinforced concrete buildings are in several cases strongly affected by the nonlinear response and possible failure of the beam-column joints. Beam-column joint inelasticity is typically due to either shear cracking and failure of the central concrete panel or bond-slip of the longitudinal steel bars. This paper proposes a new Joint with Hinges macro-element capable of simulating the most important sources of nonlinearities in the joints. It consists of a quadrilateral central panel whose rigid edges are connected to the beams' and columns' end nodes through nonlinear finite-length interfaces that represent the plastic hinge zones. The central panel deforms in shear only. The joint macro-element accounts for the nonlinear shear response of the central panel, for the bond-slip of the longitudinal rebars crossing the joint and for the nonlinear shear and flexural behavior of the plastic hinge zones of the beams and columns connected to the joint. The resulting model of the reinforced concrete frame is the assembly of non-linear Joint with Hinges macro-elements connected by elastic frame elements. The proposed formulation is applied in this paper to plane frames. Validation studies with results from available experimental tests on beam-column joint sub-assemblages show the proposed model capability to predict the hysteretic responses and the failure mechanisms of connections with unreinforced joints and different beam reinforcement ratios.

KEYWORDS

Reinforced-concrete frame, beam-column joint, joint element, macro-modeling, seismic behavior, fibre section, bond-slip

INTRODUCTION

Recent earthquakes worldwide have shown the high vulnerability of reinforced concrete (RC) beam-column joints in RC buildings not designed to resist seismic actions or designed according to old codes [Ghosh 1995] [Celik 1999] [Doğangün 2004] [Masi et al. 2017]. The failure of few joints can cause severe structural damage up to complete building collapse, drastically limiting drift and energy dissipation capacities. It follows that the prediction and prevention of joint failures are crucial aspects in the evaluation and reduction of the seismic vulnerability of non-conforming RC buildings.

During an earthquake beam–column joints may experience high shear stresses induced by the forces transferred by the beams and columns connected to the joint. Moreover, significant bond stresses develop at the interfaces between the concrete and the longitudinal reinforcing steel bars anchored in or passing through the joint. These stresses produce diagonal principal tension and compression stresses in the joint concrete panel that are carried by appropriately designed steel stirrups in modern code-conforming joints or by a strut-and-tie mechanism in older, unreinforced joints [Paulay et al. 1992][Paulay et al. 1978]. In the latter case, the diagonal principal stresses can lead to concrete cracking or crushing along the concrete joint panel diagonals.

A number of experimental campaigns have been carried out to investigate the ultimate strength and the corresponding failure modes of beam-column joints without shear reinforcement. The main parameters studied in these experimental tests are the joint geometry, the concrete strength and the beam reinforcement ratio, in order to evaluate their influence on the joints' nonlinear cyclical behaviour. Experimental tests have been typically performed on structural sub-assemblages reproducing internal [Alire 2002][Walker 2001][Melo et al. 2014] or external [Pantelides et al. 2017]

[De Risi et al. 2016] [De Risi et al. 2017] beam-column joints. Extensive database of experimental tests on beam-column RC sub-assemblages can be found in [Mitra and Lowes 2007] [Kim et al. 2007] [Parate et al. 2019].

Two main mechanisms are typically observed: *shear crisis* of the concrete panel or beam longitudinal steel *rebars crisis*. The latter inelastic mechanism is associated with either rebar yielding (when beams have low reinforcement ratios) or bond-slip of the rebars anchored in the joint (due to inadequate anchorage lengths within the joint).

Current seismic codes [ACI 318-19][EN 2004][NTC 2018] prescribe specific details and design procedures in order to avoid the local failure of beam-column joints. Adequate anchorage lengths of the steel rebars within the joint area and shear reinforcement along the joint height are prescribed to avoid bond and shear failures, respectively. On the other hand, many old RC structures in high-seismic regions lack these construction details.

The seismic vulnerability assessment of existing RC buildings should rely on models capable of reproducing the main sources of nonlinearities in the frame. However, few models are available for beam-column joints, thus joint failure is usually checked in the post-processing phase of nonlinear analyses. With this approach, however, the analyses fail to trace the frame response after joint failure occurs. Beam-column joint elements should account for both deformability and strength of the joints. Several models have been proposed for the monotonic and cyclic behaviour of beams-columns joints [Lowes et al. 2003] [Anderson et al. 2008] [Lima et al. 2017]. Critical reviews of the literature models are reported in [Celik et al. 2008] and [Sharma et al. 2011]. Typically, nonlinear joint elements are connected to nonlinear frame elements that account for the nonlinear response of the plastic zones at the ends of the beams and columns connected to the joint [Izzudin et al. 1994][Spacone et al. 1996][Pantò et. al 2019].

The beam-column joint models proposed to date can be classified into three categories: (i) lumped plasticity models; (ii) multi-spring models and (iii) finite element-based models. For frame analysis, only the first two categories are of interest. The first one includes early attempts to account for the inelastic behaviour of the joint through plastic hinges located at the beams' ends. Different moment-rotation hysteretic constitutive laws have been proposed and empirically calibrated to fit experimental tests [Otani 1974] [Kim and LaFave 2008]. [Fillipou et al. 1983] proposed a model that includes the effects of bond deterioration on the joint hysteretic behaviour. Their model consists of a concentrated rotational spring located at each girder end. [Kunnath et al. 1995] modified the flexural capacities of the beams to account for insufficient bar anchorage length and inadequate joint shear capacity. Even when properly calibrated, these models cannot separate the joint rigid rotation from the central panel shear deformations. It is thus difficult to separate bond-slip and shear failure mechanisms.

To explicitly simulate the joint shear deformations, non-linear rotational springs [Lima et al. 2017][Pampanin et al 2003][Biddah et al. 2011] connected to the frame elements by rigid links have been proposed. The spring moment–rotation law is calibrated from experimental results, assuming the spring rotation to be equal to the joint shear deformation. More recent developments are proposed in [Sharma et al. 2011] and [Metelli et al. 2015] where translational and rotational springs are placed in series in order to simulate the non-linear behaviour of the joint as well as the shear collapse of the frame elements, including bond-slip of the longitudinal rebars. In these lumped plasticity models, the joint is typically modelled as having zero dimensions.

More sophisticated *multi-spring models* with finite dimensions have also been proposed. The joint core is modelled by a 2D continuous shear-deformable panel in [Elmorsi et al. 2000][Lowes et al. 2003][Mulas 2004] or by a discrete quadrilateral whose deformability is governed by uni-dimensional, translational or rotational, springs [Yousef et al. 2001][Altoontash et al. 2004][Shin et al. 2004]. In [Yousef et al. 2001] two diagonal springs simulate the joint panel tie-and-strut mechanism while three uniaxial springs (normal to each panel edge) simulate the non-linear flexural interaction between the joint and the elastic beam elements. In [Altoontash et al. 2004] a central rotational spring located at the centroid of the quadrilateral governs the joint shear behaviour, and four nodes located at the quadrilateral edges connect the joint to the frame elements. In [Shin et al. 2004] three parallel rotational springs located at one vertex of the quadrilateral simulate its shear deformability. Four rotational springs at the centre of each edge are connected to the frame elements in order to simulate the additional deformability due to the bond-slip of the steel bars. An attempt to simulate the complex bar-slip mechanism of longitudinal steel bars within the central joint is represented by the macro joint model proposed by [Zhao et al. 2019].

The model proposed in [Lowes et al. 2003], later calibrated and validated in [Lowes et al. 2004], consists of a 4-node panel surrounded by 4 zero-length interfaces each consisting of two uniaxial springs that simulate the bond-slip of the longitudinal bars and one uniaxial spring that simulates the shear deformation of the adjacent frame element. The mechanical behaviour of the model originally followed the modified compression field theory [Vecchio et al. 1986] for the simulation of ductile RC joints. The model was later updated in [Mitra et al. 2007] by introducing two diagonal springs to simulate the shear behaviour of joints without transverse reinforcement. The springs have a tri-linear constitutive law with pinching hysteretic behaviour. A more accurate, experimentally calibrated, cyclic constitutive law is proposed in [Anderson et al. 2008]. The modelling strategy proposed in [Mitra et al 2007] can effectively reproduce the non-linear cyclic response of RC joints, both in terms of ultimate strength and stiffness degradation,

thus predicting the main interactions between the joint and the connected elements. It is implemented in the open source structural code *OpenSees* [Mc Kenna 2010] and can be used to analyse multi-storey frame buildings with a reasonable computational effort. The general limitation of multi-spring models is the spring calibration, which requires procedures mainly based on empirical formulations.

A new joint macro-element is proposed in this paper. The idea is to lump all the main nonlinearities that develop around the beam-column joint (joint panel deformations and beams' and columns' plastic hinge deformations) in the new *JointwithHinges* macro-element. In the proposed approach, the joints are connected through elastic frame elements, unless other sources of nonlinearities along the beams' and columns' spans need to be modeled, in which case nonlinear frame elements can be used. A quadrilateral element with finite dimensions and rigid edges is used to simulate the behavior of the joint panel. Finite-length interfaces connect the quadrilateral element to the adjacent beams and columns. These interfaces account for the flexural and shear deformations of the plastic hinge zones connected to the joint, as well as for the bond-slip of the longitudinal bars embedded in the joint.

Following this introduction, a general description of the proposed model is presented. The model kinematics are then discussed followed by the derivation of the element stiffness matrix and internal forces. The presentation of the nonlinear constitutive laws and their calibration completes the element formulation. Finally, the model is validated through simulations of full scale experimentally-tested specimens representing internal and external beam-column joint assemblages [Alire 2002][De Risi et al. 2016].

BEAM-COLUMN JOINT MACRO-ELEMENT

The proposed joint macro-element, or simply macro-element, derives from a plane element proposed by the first and third authors for the simulation of the non-linear behaviour of unreinforced masonry buildings [Caliò et al. 2005][Caliò et al. 2012][Pantò et al. 2017] and masonry infilled frames [Caliò et al. 2014][Pantò et al. 2018]. The basic element is a quadrilateral with rigid edges (the joint panel) plus 1D interfaces along the four edges (Figure 1). The interfaces have a finite thickness (or length) and represent the plastic hinge zones of the beams and columns connected to the joint.

The non-linear mechanical behaviour of the macro-element is governed by the normal and tangential deformations of the edge interfaces and by the in-plane deformability of the quadrilateral. Since its edges are assumed rigid, the quadrilateral can only deform in shear. The mechanical behaviour of each interface is governed by three local degrees of freedom (dofs), two translations associated with the normal and the tangential directions and a rotation. The normal displacements of the interfaces control the non-linear axial-flexural response of the plastic hinge zones while the tangent response simulates their shear behaviour. The shear behaviour of the central joint depends on a single generalised deformation parameter that governs both its deformability and its ultimate strength through a uniaxial constitutive law.

The main novelty of the proposed macro-element with respect to previously proposed models lies in the fact that it includes both the joint response and the response of the plastic hinge regions of the connected beams and columns. Also, the plastic hinge regions have finite lengths. The resulting element is named *JointWithHinges* (similarly to the *BeamWithHinges* element proposed in [Scott et al. 2006] and implemented in *OpenSees*). The normal and tangential stiffness distributions along the interfaces reproduce the behaviour of the concrete in compression/tension and shear, respectively (Figure 1). The interface (or hinge) regions are modelled using a fibre-section discretization. Constant axial strain, curvature and shear deformation are assumed along the interface length.
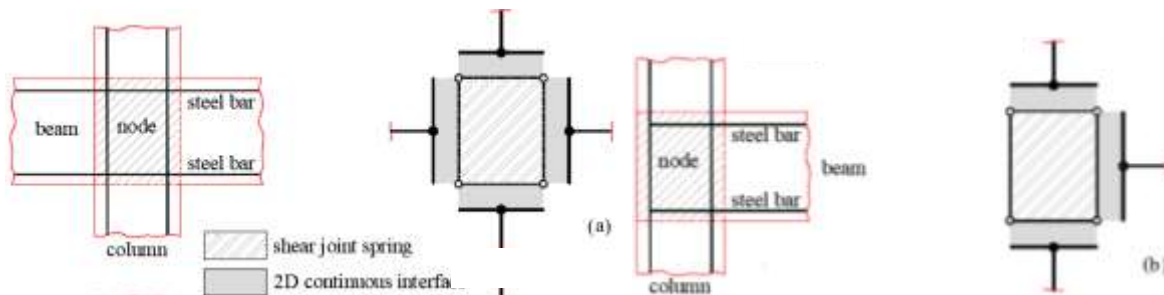

Figure 1   Macro-element representation of (a) an external and (b) an internal beam-column joint.

The reinforcing bars are simulated by fibres that lump both the cyclic behavior of the steel bars along the plastic hinge regions and the bond-slip of the bars embedded within the joint region. This feature is another novel aspect of the proposed macro-element with respect to previously proposed models, where springs simulate the bond-slip mechanism only [Lowes et al. 2003].

Figure 2 schematically represents the main mechanisms and the corresponding macro-element simulation of an external joint. Figure 2a shows concrete cracking and tension plasticity in the steel bars (due to either yielding or bond-slip), simulated by the progressive tension-softening of the continuous interface and the stiffness degradation of the bars crossing the crack, respectively. Figure 2b shows concrete crushing. This is simulated by the plastic compression deformations of the interface concrete. Figure 2c shows a shear crack in the beam, simulated by the shear mechanism of the interface. Figure 2d shows a shear crack of the joint panel, simulated by the panel diagonal nonlinear response. Because each mechanism is reproduced by a specific component of the macro-element, the definition of the capacity limits and the interpretation of the results are simplified. Also, mixed failure mechanisms, involving both the joint region and the plastic hinges, can be effectively simulated by the proposed macro-element.
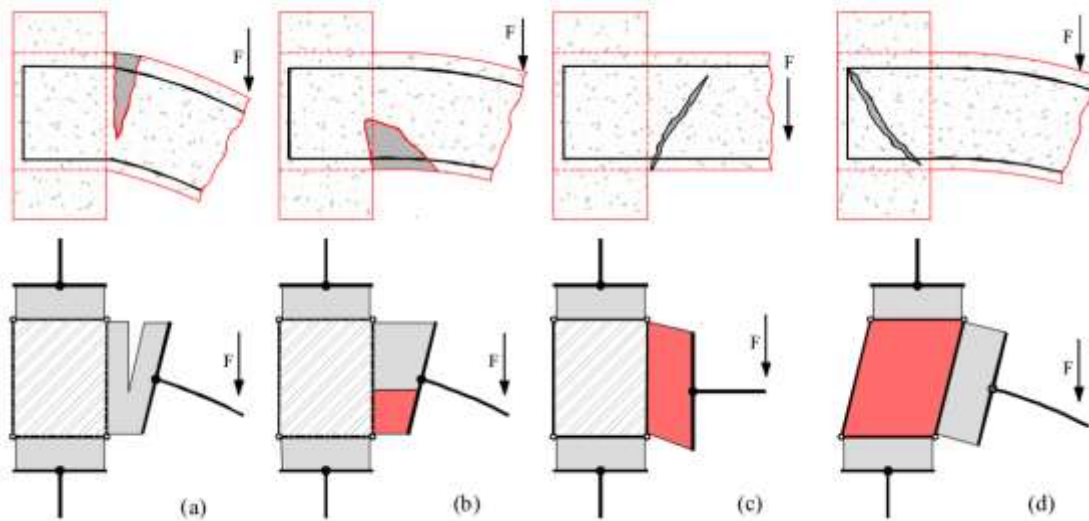

Figure 2   Main failure mechanisms of an external joint (top) and corresponding macro-element simulation (bottom): (a) concrete cracking and yielding of the steel bars; (b) beam concrete crushing; (c) beam shear failure; (d) central joint shear failure.

Irregular geometries, with different beam and/or column depths or non-alignments in the element axes can be easily described by considering the proper length and position of the interfaces with respect to the central joint (Figure 3). The interfaces' lengths are indicated as L_i with $i=1,...,4$. The central joint width (b_p) and depth (h_p) are computed as $max\{L_1; L_3\}$ and $max\{L_2; L_4\}$, respectively. The macro-element out-of-plane thickness (w_p) is the average of the out-of-plane beams' and columns' thicknesses, i.e. $w_p=\frac{1}{4}(w_{c1} + w_{c2} + w_{b1} + w_{b2})$, where subscripts c_1,c_2 and b_1,b_2 refer to the columns and beams, respsectively.
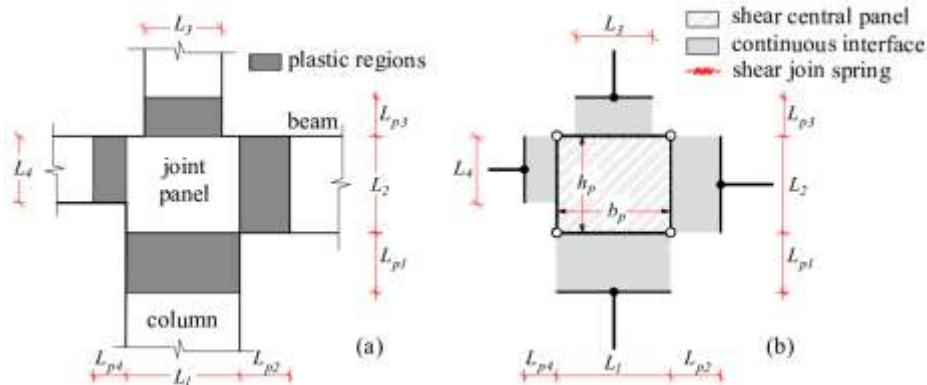

Figure 3   Macro-element modelling of an irregular beam-column joint.

The *JointWithHinges* dofs are the four dofs of the quadrilateral panel plus three dofs for each interface (shown in the next section in Figure 5), for a total of $4+3n$ dofs, where n is the number of frame elements connected to the joint. The interfaces have finite lengths ($L_{p1},..., L_{p4}$) that simulate the plastic regions of the frame elements connected to the joint macro-element. The non-linear behaviour of a plane frame structure is thus simulated through the assemblage of *JointWithHinges* elements connected to frame elements whose length is the distance between the joints' centres minus the joint panels' width and the two plastic hinge lengths. The frame elements are considered elastic in the present study, but they can be modelled as nonlinear if needed. Compared with elements with zero-length joint panels and plastic hinges, the reduced length of the frame elements (connected to the macro-elements) due to the finite sizes of the joint panels and the finite lengths of the plastic hinges removes the need for ad-hoc calibrations of the elastic element stiffness to avoid overestimation of the beams' and columns' flexibility [Ibarra et al. 2005].

Figure 4a shows a simple one-bay one-storey frame with the indication of the joint and the plastic regions located at the ends of each column (L_p^{column}) and beam (L_p^{beam}). Figure 4b shows the corresponding model with the *JointWithHinges* elements, where two articulated quadrilaterals simulate the beam-column joint panels, the joint interfaces simulate the plastic hinge regions and two interfaces connect the columns to the base supports.
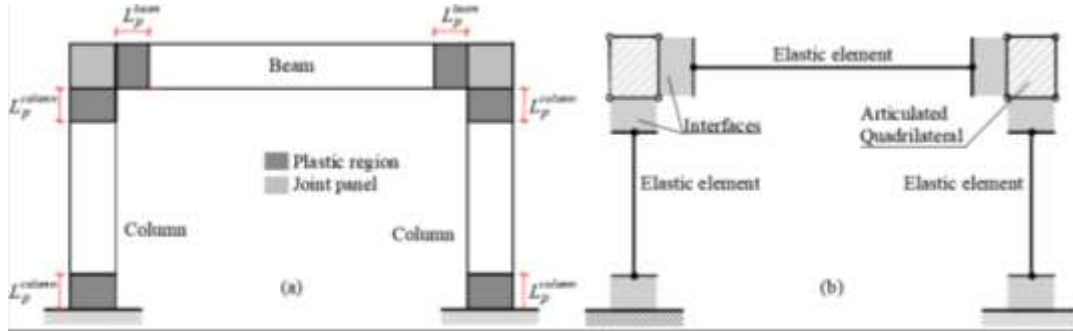

Figure 4   Simple plane frame: (a) plastic and joint regions; and (b) modelling with non-linear *JointWithHinges* elements and linear frame elements.

The proposed model presents similarities with the model proposed by [Lowes et al. 2004], modified by [Mitra et al. 2007] and later calibrated and validated in [Anderson et al. 2008]. However, the proposed element carries an important original aspect due to the inclusion of finite-length interfaces with fibre-sections connected to the edges of the finite-size joint quadrilateral. It can be classified as a hybrid model, between a pure multi-spring model and a continuous finite element model. It takes advantage of the discrete modelling approach that simulates the shear-strut mechanism within the joint panel, and of the continuous interfaces that simulate the non-linear axial/flexural/shear behaviour of the plastic hinge regions. In previous models flexural non-linearities are concentrated in the frame elements connected to the joint while the interfaces account for the local mechanisms at the joint-element interface such as bond-slip.

JOINT MACRO-ELEMENT KINEMATICS

The *JointWithHinges* macro-element has four nodes ($P_1,...P_4$ in Figure 5) located at the centre of the outer edge of the four interfaces. Each macro-element is connected to frame elements according to the standard FE connectivity procedure.

The *JointWithHinges* kinematics are governed by three dofs at each of the four nodes P_i ($u_i \quad v_i \quad \phi_i$) and four dofs ($w_1 \quad w_2 \quad w_3 \quad w_4$) associated with the rigid body motions and shear deformation of the joint panel. The joint panel is defined by the four corner points $J_1,..,J_4$. Figure 5 shows an internal joint with sixteen dofs. Vector **U** in Eq. (1) defines all the element dofs (Figure 5a) while vector **F** of Eq. (2) defines the corresponding dual forces (Figure 5b). Figure 5a also shows the local reference systems associated with the panel (e_{px}, e_{py}) and the four interfaces (e_{ix}, e_{iy}).

$$\mathbf{U} = [u_1 \quad v_1 \quad \varphi_1 \quad u_2 \quad v_2 \quad \varphi_2 \quad u_3 \quad v_3 \quad \varphi_3 \quad u_4 \quad v_4 \quad \varphi_4 \quad w_1 \quad w_2 \quad w_3 \quad w_4] \tag{1}$$

$$\mathbf{F} = [N_1 \quad T_1 \quad M_1 \quad N_2 \quad T_2 \quad M_2 \quad N_3 \quad T_3 \quad M_3 \quad N_4 \quad T_4 \quad M_4 \quad F_1 \quad F_2 \quad F_3 \quad F_4] \tag{2}$$
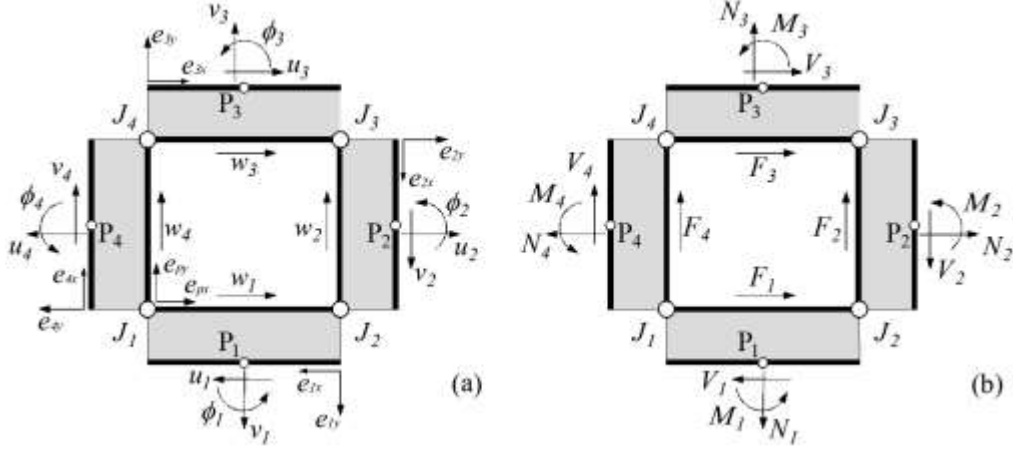
Figure 5 *JointWithHinges* **Macro-element (a) displacements and (b) dual forces.**

In order to describe the kinematics of the generic interface a local node (P$_q$) is introduced in the centre of each panel edge, as shown in Figure 6a. For simplicity, subscript for interface i is dropped. The displacements of P$_q$ are related to the panel dofs. In Figure 6a reference is made to a partial length interface (i.e the interface width is smaller than that of the corresponding joint edge). Each interface is governed by six dofs, three $\left(u_q \quad v_q \quad \phi_q \right)$ associated with the panel edge dofs, and three $(u \quad v \quad \phi)$ with the global node P. In Figure 6a J$_I$ and J$_F$ indicate the interface starting and end point, respectively, L is the interface width and L_p the interface thickness. Three generalised deformations (or relative displacements) define the interface deformations: the normal (dv_G) and longitudinal (du_G) deformations and the relative rotation $(d\phi)$, as shown in Figure 6b.
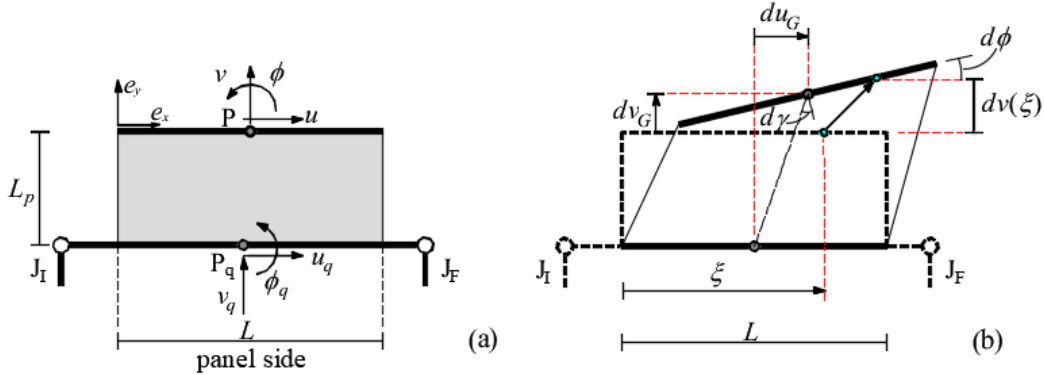

Figure 6 **Interface (a) local dofs and (b) generalised deformations.**

From Figure 6b the normal deformation $dv(\xi)$ at the outer edge point of abscissa $0 \leq \xi \leq 1$ and the average shear drift $d\gamma$ are given by the following kinematic equation:

$$\mathbf{d}(\xi) = \begin{bmatrix} d\gamma \\ dv(\xi) \end{bmatrix} = \begin{bmatrix} -1 & 0 & -\alpha L_p & 1 & 0 & (1-\alpha)L_p \\ 0 & 1 & -L(\xi - 1/2) & 0 & -1 & L(\xi - 1/2) \end{bmatrix} \begin{bmatrix} u_q \\ v_q \\ \phi_q \\ u \\ v \\ \phi \end{bmatrix} = \mathbf{B}(\xi)\mathbf{u} \tag{3}$$

where α $(0 \leq \alpha \leq 1)$ identifies the center of rotation of the plastic hinge. This parameter allows to consider the kinematic coupling between the rotation and the longitudinal (shear) displacement of the interface. $\alpha = 0$, as assumed in this paper, indicates rotation around the joint panel edge. Intermediate values of α indicate different positions of the center of rotation.

If subscript i identifies the generic interface, Eq. (3) becomes

$$\mathbf{d}_i(\xi) = \mathbf{B}_i(\xi)\mathbf{u}_i \tag{4}$$

If $\mathbf{A}_i$ is the matrix that maps the macro-element dofs into the interface dofs (that is $\mathbf{u}_i = \mathbf{A}_i\mathbf{U}$) Eq. (4) becomes

$$\mathbf{d}_i(\xi) = \mathbf{B}_i(\xi)\mathbf{A}_i\mathbf{U} \tag{5}$$

It is assumed that the panel joint undergoes pure shear strain γ with a uniform stress distribution τ governed by a single Lagrangian parameter Δ_d associated with the panel diagonal elongation (Figure 7). Δ_d is expressed as a function of the panel internal dofs:

$$\Delta_d = [-cos(\alpha) \quad sin(\alpha) \quad cos(\alpha) \quad -sin(\alpha)]\begin{bmatrix} w_1 \\ w_2 \\ w_3 \\ w_4 \end{bmatrix} = \mathbf{B}_p\mathbf{A}_p\mathbf{U} \tag{6}$$

where $\alpha = \arctan(h_p/b_p)$, and $\mathbf{A}_p$ is a 4×16 matrix $\mathbf{A}_p = [\mathbf{0}_{4x12} \quad \mathbf{I}_{4x4}]$ that maps the element dofs ($\mathbf{U}$) into the four panel displacements w_i.
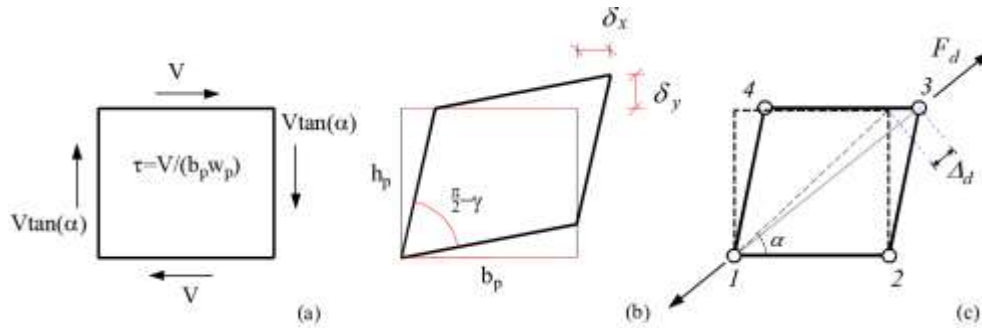

Figure 7   Joint central panel generalised shear deformation.

The central joint shear behaviour is governed by a uniaxial constitutive law (described later) between the local shear stress (τ) and the local shear strain (γ). The shear stress is $\tau = V/(b_pw_p)$, where V is the shear force acting on the joint horizontal edges. The panel shear strain is $\gamma = \delta_x/h_p + \delta_y/b_p$, where $\delta_x = w_3 - w_1$ and $\delta_y = w_2 - w_4$ are the horizontal and vertical drifts between the opposite joint edges, respectively (see Figure 7b). The diagonal elongation Δ_d and the dual force F_d, obtained by integrating the uniform shear stress and strain in the joint panel, are:

$$F_d = \tau b_pw_p/\cos(\alpha)$$
$$\Delta_d = \gamma h_p\cos(\alpha) \tag{7}$$

JOINT MACRO-ELEMENT STIFFNESS MATRIX AND NODAL FORCES

The stiffness matrix and the nodal forces of the joint macro-element are evaluated using a uniaxial law for the panel shear and a fibre-section discretization for the interface cross sections. The formulation is general, though the current implementation uses the tangent stiffness.

Since the panel shear deformation is related to a single Lagrangian parameter Δ_d, the corresponding mechanical behaviour is controlled by a single tangent stiffness term k_d.

Curvature, axial and shear deformations are assumed constant along the plastic hinge (interface) length thus a single section describes the hinge response. Each section is discretised into n_b steel fibres and n_c concrete fibres. The steel fibres have normal strains only, while the concrete fibres may in the general case have both normal and tangential strains. The interface constant shear strain is the angular shear strain γ between the two interface edges (Figure 6).

The *JointWithHinges* 16×16 stiffness matrix $\mathbf{K}$ is obtained by enforcing the virtual work principle. The internal virtual work done in the interfaces and in the joint panel is:

$$\delta L_{int} = k_d\Delta_d\delta\Delta_d + \sum_{i=1}^{4}\left[\sum_{f=1}^{nfi}\left(\mathbf{d}_i^{\mathrm{T}}(\xi_f)\mathbf{k}_f(\xi_f)\delta\mathbf{d}_i(\xi_f)\right)\right] \tag{8}$$

where subscript f indicates the generic fibre, nfi is the total number of fibres in section i and ξ_f indicates the fibre location. For concrete

$$\mathbf{k}_f(\xi_f) = \begin{bmatrix} k_n(\xi_f) & k_{ns}(\xi_f) \\ k_{sn}(\xi_f) & k_s(\xi_f) \end{bmatrix} \tag{9}$$

where subscripts n and s indicate normal and tangential, respectively. For steel

$$\mathbf{k}_f(\xi_f) = \begin{bmatrix} k_b(\xi_f) & 0 \\ 0 & 0 \end{bmatrix} \tag{10}$$

In the current model implementation, the axial-shear interaction in the concrete fibers is ignored. Eq (9) thus becomes:

$$\mathbf{k}_f(\xi_f) = \begin{bmatrix} k_n(\xi_f) & 0 \\ 0 & k_s(\xi_f) \end{bmatrix} \tag{11}$$

and the term $k_s(\xi_f)$ is constant over the section. A generalised V-γ law (with $\gamma = du/L_p$) is used. This approach is similar to that proposed in [Marini et al. 2006] and implemented in *OpenSees* with the *SectionAggregate* command.

Substituting Eqs. (5) and (6), Eq. (8) becomes:

$$\delta L_{int} = \mathbf{U}^T \left\{ \left[\mathbf{A}_p^T \mathbf{B}_p^T k_d \mathbf{B}_p \mathbf{A}_p \right] + \sum_{i=1}^{4} \left[\mathbf{A}_i^T \sum_{f=1}^{nfi} \left(\mathbf{B}_i^T(\xi_f) \mathbf{k}_f(\xi_f) \mathbf{B}_i(\xi_f) \right) \mathbf{A}_i \right] \right\} \delta\mathbf{U} \tag{12}$$

Hence, the stiffness matrix is

$$\mathbf{K} = \left[\mathbf{A}_p^T \mathbf{B}_p^T k_d \mathbf{B}_p \mathbf{A}_p \right] + \sum_{i=1}^{4} \left[\mathbf{A}_i^T \sum_{f=1}^{nfi} \left(\mathbf{B}_i^T(\xi_f) \mathbf{k}_f(\xi_f) \mathbf{B}_i(\xi_f) \right) \mathbf{A}_i \right] \tag{13}$$

For given nodal displacements, the element forces ($\mathbf{F}$) are the sum of all the fibre forces $\mathbf{F}_i(\xi_f)$ of the four interfaces plus the force F_d along the panel joint diagonal. The element nodal forces are then:

$$\mathbf{F} = F_d \mathbf{B}_p \mathbf{A}_p + \sum_{i=1}^{4} \left[\sum_{f=1}^{nfi} \mathbf{F}_i^T(\xi_f) \mathbf{B}_i(\xi_f) \mathbf{A}_i \right] \tag{14}$$

CONSTITUTIVE LAWS

Given the proposed model components, four constitutive laws are needed, two for the interface concrete and steel fibres, one for the interface shear response and one for the joint panel shear response.

Concrete and Steel Fiber Constitutive Laws

For concrete fibres, a general formulation would require a multiaxial constitutive law to account for both normal and tangential stresses. This approach is beyond the scope of this initial work that focuses on the macro-model formulation. Thus, in this study the shear response of the interfaces is assumed uncoupled from the normal stresses, as shown in Eq. (11). The shear behavior of the hinges connected to the joint is assumed linear-elastic. Further developments are under way to include the nonlinear shear behavior of the plastic hinge regions. The well-known [Kent et al. 1971] model (*Concrete01* law in *OpenSees* [Mc Kenna et al. 2010]) is used for the concrete normal stresses. The concrete tensile strength is neglected. The fibers' stresses and strains are assumed constant over the fiber length L_f, which is assumed equal to the interface thickness L_p. The compression softening branch is calibrated considering [Coleman and Spacone 2001]. The generic fibre force F_f and elongation u_f are $F_f = f_f A_f$ and $u_f = \varepsilon_f L_p$, respectively, with f_f and A_f fibre stress and area, respectively. The fibre normal tangent stiffness term in Eqs. 8 and 9 is $k_n(\xi) = \left(\frac{\partial f}{\partial \varepsilon} \right)_\xi \frac{A_f}{L_p}$.

The elastic shear stiffness is $k_s(\xi) = \frac{GA_s}{L_p}$, where G is the shear modulus and A_s the shear area.

As for the steel bar, experimental observations [Viawanthanatepa et al. 1979] show that the local nonlinear response of the beam-to-joint interface regions can be affected by the slip mechanism of the steel bars, even in the presence of an adequate anchorage length, due to damage in the joint panel. Moreover, once the slip occurs or heavy concrete damage takes place, buckling of the steel bars under compression can also occur due to the loss of confinement associated with damage concentration. Bar buckling is not considered in this paper. Following a phenomenological approach these effects can be simulated by introducing a pinching effect in the cyclic constitutive law. The bar nonlinear behaviour is described by the model by [Braga et al. 2012], later validated by [D'Amato et al. 2012], and is based on a quadrilinear backbone curve that accounts for both slip and yielding of the bar.

The concept is rather simple: the slip locally decreases the stiffness of the steel loading-reloading branches. An elastic-perfectly plastic local bond slip law is assumed that is governed by a tangential limit strength τ_{lim} and bond-slip elastic

stiffness k_s. Two limit states are identified: the yield state (u_y, F_y) corresponding to the activation of the steel-concrete slip at the loaded end of the bar; the ultimate state (u_u, F_u) corresponding to the achievement of the limit bond-slip tangential stress for all the anchorage (L_a) or critical (L_0) length of the bar or the attainment of its yield limit. The expressions of F_y are reported in Eq. (15) where $L_0 = \sqrt{3E_sD/(2k_s)}$ [Braga et al. 2012], σ_s is the steel yielding strength and D is the bar diameter. The peak force and the corresponding displacement are computed according to Eq. (16), as the minimum between the ultimate strength associated with the bond-slid [Braga et al. 2012] and the steel yield stress. After u_u a horizontal branch ensues up to the ultimate displacement capacity (u_{cr}). Beyond u_{cr}, a linear softening branch drops down to the residual force and the corresponding displacement (u_r, F_r), as shown in Figure 8.

$$F_y = \frac{\pi}{2}\tau_{lim}DL_0 \qquad\qquad if \ \ L_a \geq L_0 \ ;$$
$$F_y = \frac{\pi}{2}\tau_{lim}DL_a \left[\frac{3E_sD\tau_{lim}/k_s - 2L_a^2\tau_{lim}}{3E_sD\tau_{lim}/k_s + 4L_a^2\tau_{lim}}\right] \ \ if \ \ L_a < L_0 \qquad\qquad (15)$$

$$u_u = \frac{\tau_{lim}}{k_s} + 2\frac{\tau_{lim}L^2}{DE_s} \ ; \ \ F_u = min\{\sigma_s\pi D^2/4 \ ; \ \ \tau_{lim}\pi DL\} \qquad\qquad (16)$$

If the limit strength is related to the bond-slip, the parameters governing the softening branch are assumed $F_r = 0.3F_u$ and $u_{cr} = 2/3u_r$, while the ultimate slip displacement is $u_r = 3.0 \ mm$. If the limit strength is related to the bar yielding, u_{cr} is due to rupture of the steel bar assumed at 10% of the fiber-bar length.

The steel constitutive law (Figure 8) is obtained by adding the deformations associated with the bar bond-slip embedded in the joint and that of the steel bar (whose behavior is assumed elastic-perfectly plastic) within the plastic hinge. The strain and strength parameters characterizing the back-bone curve are summarized in Table 1.
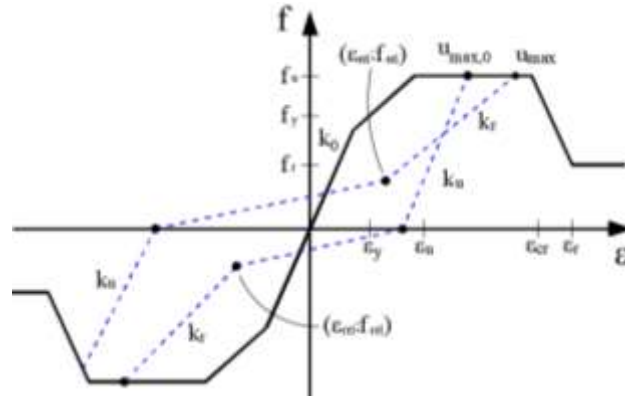

Figure 8   Steel constitutive law

Table 1: Mechanical parameters of the steel constitutive law.

f_y [MPa]	f_u [MPa]	f_r [MPa]		ε_y [-]	ε_u [-]	ε_{cr} [-]		ε_r [-]	
		Y	BS			Y	BS	Y	BS
$\frac{4F_y}{D^2\pi}$	$min\left\{\sigma_s; \frac{4F_u}{D^2\pi}\right\}$	0.0	$0.3F_u$	$\frac{u_y}{L_p} + \frac{F_y}{EA}$	$\varepsilon_{us}+\varepsilon_{yBS}+\varepsilon_{uBS}$	0.01	2.0mm/L_p	0.01	3.0mm/L_p

where: $\varepsilon_{us} = 4f_u / E_sD^2\pi$, $\varepsilon_{yBS} = u_y / L_p$, $\varepsilon_{uBS} = D^2\pi(u_u - u_y)(f_u - f_y) / [4L_p(F_u - F_y)]$;
Y = material yield failure mode; BS = bond-slip failure mode

The cyclic response is modelled *in OpenSees* [40] with *Pinching04* uniaxial material. This law has different unloading/reloading stiffness and a central branch (*pinching*) where the stress does not increase during reloading. The initial and final points of the pinching phase are fixed as ratios of the maximum displacement achieved at the previous load cycles [Mitra et al. 2004]. In the numerical applications, the unloading phase ends at zero unloading force, while the reloading phase $(u_{rel}; F_{rel})$ starts at 25% of the maximum displacement and force achieved at the previous cycles. Stiffness degradation is modelled following [Lowes et al. 2003]. The unloading stiffness is $k_u = k_0/(1 - \delta_k)$, where k_0 is the initial unloading stiffness, $\delta_k = \alpha_1(u_{max,0}/u_r)^{\alpha_3} \leq \delta_{k,lim}$ is the stiffness damage index and $u_{max,0}$ is the maximum displacement at unloading. Degradation of the reloading stiffness k_r is computed by increasing the

displacement demand at the end of reloading $u_{max} = u_{max,0}(1 + \delta_u)$, where $\delta_u = \beta_1(u_{max}/u_r)^{\beta_3} \leq \delta_{u,lim}$ is the reloading stiffness damage index. Following [Lowes et al. 2003] the following parameters are considered for the unloading stiffness degradation: $\alpha_1 = 0.3$; $\alpha_3 = 0.1$; $\delta_{k,lim} = 0.4$ and $\beta_1 = 0.6$; $\beta_3 = 0.2$; $\delta_{u,lim} = 0.25$. Following [Lowes et al. 2004] and [Viawanthanatepa et al. 1979] $\tau_{lim} = 1.5\sqrt{f_c}$, and $k_s = 10\tau_{lim}(MPa/mm)$.

Joint Panel Shear Behavior

Following the assumption of uniform shear stress and strain distributions in the central joint the joint panel of Figure 7 is governed by a $\tau - \gamma$ uniaxial constitutive law.

Several models have been proposed both for interior and exterior joints, based on mechanical formulations [Lowes et. al 2003] or statistical fitting of experimental data [Vollum et al. 1999][Jeon et al. 2014]. For interior joints, an early model is proposed in [Paulay et al. 1992], where the unreinforced joint ultimate strength is related to the compression strength of the diagonal strut. More recently [Hwang et al. 2002] proposed a strut-and-tie equivalent model while [Kim et al. 2007] proposed a joint shear strength and deformation model for different types of RC beam-column connections based on a statistical analyses of a wide range of experimental tests. For exterior joints, the models proposed by [Scott et al. 1994] and [Vollum et al. 2008], based on a single diagonal strut and on a strut-and-tie scheme, respectively, are worth mentioning together with the model proposed by [Bakir et al. 2002], which is based on a statistical fitting approach. More recently, [Park et al. 2013] proposed a double-strut mechanical model and [Jeon et al. 2014] proposed a model based on multiple linear regression and advanced machine-learning methods. Both of these models explicitly take into account the longitudinal steel reinforcement ratio in the beams and its influence on the joint failure mechanism. The uniaxial *Pinching04* material in *OpenSees* [McKenna 2010] is used (Figure 9).
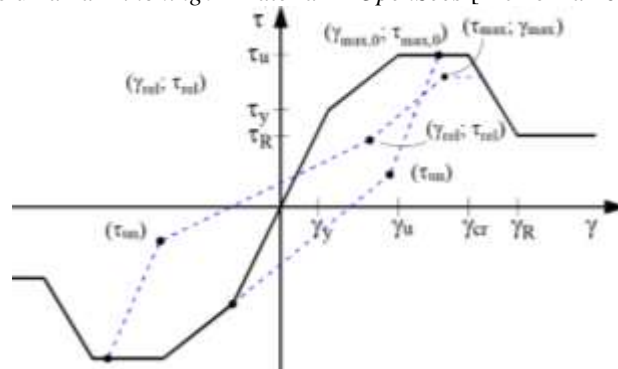

Figure 9   Joint panel shear constitutive law

The main parameters are selected based on [De Risi et al. 2016], [Celik et al. 2008], [Lowes et al. 2004] and [Vollum et al. 2008]. The first branch, up to concrete cracking (τ_y, γ_y), identifies the joint undamaged elastic response and is followed by the pre-peak branch up to the ultimate state (τ_u, γ_u) that corresponds to the joint failure. The critical drift (γ_{cr}) corresponding to the beginning of concrete spalling is identified by the initial point of the softening branch that ends at the residual strength point (τ_R, γ_R). This softening branch is difficult to calibrate due to the lack of reliable experimental data since concrete spalling (Figure 10) makes it difficult to find an accurate measure of the generalised shear deformation of the joint after the ultimate state.
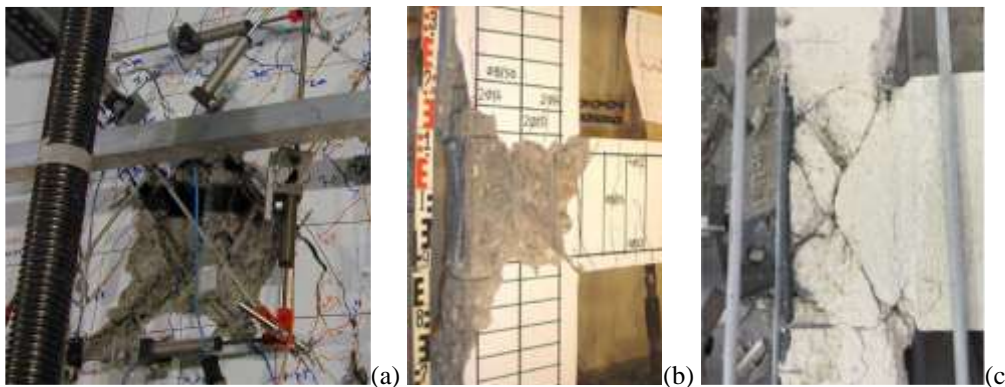

Figure 10   Experimentally observed severe concrete spalling: (a) [Walker 2001]**; (b)** [Pantelides et al. 2017] **and (c)** [De Risi et al. 2016]**.**

This constitutive law is calibrated differently for interior and external joints. More specifically, the envelopes proposed in [Anderson et al. 2008], based on tests performed by [Alire 2002] and [Walker 2001], are considered for internal joints while the envelopes of the exterior joint are calibrated following [Pantelides et al. 2017], [De Risi et al. 2016,] and [De Risi et al. 2017].Following [Anderson et al. 2008] the internal joints' ultimate strength is assumed to depend on the concrete compression strength and the ultimate beam bending moments associated with yielding of the steel bars:

$$\tau_u = 0.95 \frac{T_1 + T_2}{A_p} = 0.95 \frac{1.25 f_y (A_{s1} + A_{s2})}{A_p} \leq 1.95 \sqrt{f_c} \tag{17}$$

where f_c is the concrete compressive strength in MPa, T_1 and T_2 are the maximum tensile forces in the left and right beam, respectively, A_{s1} and A_{s2} the beam areas of the steel bars in tension, f_y the steel yield stress and $A_p = b_p w_p$ the joint horizontal cross section.

For exterior joints, the formulation by [Vollum et al. 1999], as modified by [Lima et al. 2017], is considered. The ultimate joint shear strength, expressed as a function of the joint aspect ratio and of the concrete compression strength, is reported in Eq. (18), where β assumed equal to 0.8. The upper bound limit strength $\tau_{u,max}$ accounts for the influence of the beam reinforcing ratio on the joint strength. This limit is set to 75% of the joint shear index defined in [Park et al. 2012], as reported in Eq. (19), where A_s represents the tension steel area, H the column inflexion length and h_b the beam depth. The latter criterion allows to fit the ultimate experimental strengths obtained by [De Risi et al. 2017] on specimens with different aspect and beam reinforcing ratios. Finally, the yield shear-stress and the corresponding strain limits are found based on the experimental data reported in [Yousef et al. 2001] and [Mitra et al. 2007]. The yield stress is found as a function of the concrete compression strength while the residual strength is taken as a percentage of the peak-strength. Fixed values of limit drifts are considered for each limit state. They are calibrated differently for internal and external joints. The parameters of the envelope curve are summarized in Table 2.

$$\tau_u = 0.822 \times 0.624 \beta \left[1 + 0.555 \left(2 - \frac{h_p}{b_p} \right) \right] \sqrt{f_c} \leq \tau_{u,max} \tag{18}$$

$$\tau_{u,max} = \frac{3}{4} \frac{A_s f_y}{b_p w_p \sqrt{f_c}} \left[1 - 0.85 \frac{h_b}{H} \right] \tag{19}$$

Table 2: Mechanical parameters of the joint panel shear constitutive law.

	τ_y [MPa]	τ_u [MPa]	τ_R/τ_u [-]	γ_y [%]	γ_u [%]	γ_{cr} [%]	γ_R [%]
Internal Joints	$0.48(f_c)^{0.5}$	Eq. (17)	0.70	0.10	0.60	2.00	3.00
Exterior Joints	$0.35(f_c)^{0.5}$	Eq. (18)	0.40	0.05	0.42	1.00	3.80

Different unloading/reloading stiffness and pinching effects are considered for the joint cyclic shear response according to [Shin et al. 2004] [Lowes et al. 2004]. The shear strain at which reloading (γ_{rel}; τ_{rel}) starts is assumed as 25% of the maximum history shear strain and 50% of the maximum shear stress, respectively. The unloading stiffness is equal to the initial stiffness, while degradation of the reloading stiffness and strength is included in the model. Unloading ends at τ_{un} equal to 50% and 25% of the shear stress achieved at unloading for internal and external joints, respectively.

Material damage is ruled by two damage indexes δ_d and δ_f. The current branch maximum stress and strain on the envelope curve τ_{max} and γ_{max} are functions of the damage indexes and of the maximum stress $(\tau_{max})_0$ and strain $(\gamma_{max})_0$ reached in the previous cycles: $\tau_{max} = (\tau_{max})_0 (1 - \delta_f)$ and $\gamma_{max} = (\gamma_{max})_0 (1 + \delta_d)$. Each damage index depends on the maximum history deformation (γ_{max}) and cumulated energy (E_c). According to the formulation reported in [Lowes et al. 2003], the two indexes are $\delta_j = \alpha_{j1} (\gamma_{max}/\gamma_R)^{\alpha_{j3}} + \alpha_{j2} (\alpha_{j5} E_c / E_u)^{\alpha_{j4}} \leq \delta_{j,lim}$ where $j = d, k$ and γ_R, E_u are the ultimate deformation and ultimate energy corresponding to a monotonic loading process, respectively. The following values (based on [Lowes et al. 2003]) are considered for the deformation and force damage: α_{d1}=0.12; α_{d2}=0.00; α_{d3}=0.23; α_{d4}=0.00; α_{d5}=0.00; $\delta_{d,lim}$=0.95 - α_{f1}=1.11; α_{f1}=0.0; α_{f3}=0.32; α_{f4}=0.10; α_{f5}=10; $\delta_{f,lim}$=0.125.

MODEL VALIDATION

The following applications intend to show the proposed model capability to reproduce the different failure mechanisms that can occur when a beam-column joint is subjected to cyclic loads. Results from cyclic experimental tests and numerical simulations are compared. The analyses were performed using the computational framework *OpenSees*. In the displacement-controlled simulations, the interface (or plastic hinge) length is assumed equal to the element cross-section depth. The concrete layers are 5 cm deep. The frame elements connected to the *JointWithHinges* are modelled through the "*elasticBeamColumn*" of *OpenSees* with the section full area and inertia and concrete Young modulus reduced by 50% to simulate section cracking. The anchorage length of the longitudinal bars is computed as the joint width plus the plastic hinge length of the beam (or column) on the other side, if present. In external joints, the beam bars' anchorage length is incremented by 10 cm to account for the hook contribution.

Interior Beam-Column Joint

The experimental research considered here refers to a large experimental campaign on the response of concrete joints without transverse reinforcement described in [Alire 2002] and [Walker 2001 Lehman et al. 2004]. Eleven beam-column joint sub-assemblages were tested using the experimental test setup shown in Figure 11. All specimens have the same geometry but different beam/column steel reinforcements and concrete strength. They exhibited different joint panel shear as well as different beam flexural responses. Cyclic displacements were imposed at the beams' free ends. A constant axial load equal to 10% of the column ultimate compression ($P=641$ kN) was applied at the column's top. In the tests labelled *SCDH* the applied displacement history consists of sets of cycles of increasing amplitude. In each set, made of three equal amplitude cycles, the displacements are 30% larger than those of the previous one.
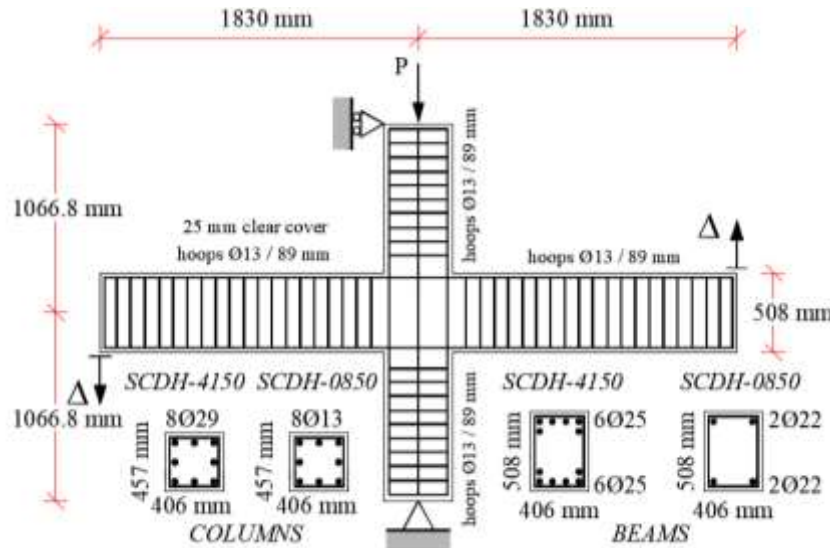

Figure 11   Geometric test layout and steel reinforcement.

The tests on specimens *SCDH-4150* and *SCDH-0850*, characterised by joint-shear and beam-flexural failure, respectively, were simulated. Figure 11 reports the test layout, the specimen geometry and the steel reinforcement. Table 3 summarises the mechanical parameters used in the analyses, where f_c and f_R denote the peak and residual concrete compression strength, respectively, and ε_0 and ε_{cu} the corresponding strains. The failure type depends on the amount of longitudinal reinforcement in the beams.

Table 3: Material parameters of specimens SCDH-4150 and SCDH-0850 ([10][11])

Concrete				Steel bars		
f_c [MPa]	f_R [MPa]	ε_0 [-]	ε_u [-]	f_y [MPa]	E_s [Ma]	ε_{su} [-]
34.5	6.8	0.0022	0.02	462	200000	0.1

During the tests, the imposed global drift (that is the displacement normalized with respect to the beam length) and the column shear were monitored. The local shear strain of the central joint was measured by a set of vertical,

horizontal and diagonal LVDTs. In specimen SCDH-0850 damage started at the joint perimeter, due to yielding of the beam bars, at 0.42% drift. Diagonal cracking of the central joint appeared at 2.0% drift while the peak-strength was reached at 4.0% drift. Joint failure, identified by the concrete spalling in the central part of the joint, was reported at 5% drift. In specimen SCDH-4150 damage started at 1.75% drift following spalling in the central joint concrete cover. The peak-stress was reached at 2% drift, when extreme concrete spalling at the central joint and yielding of the beam bars were observed.

The comparison between experimental and numerical results obtained using the proposed *JointWithHinges* element are shown in Figure 12 in terms of column shear force versus imposed beam drift. The model predicts well the global response of the system with a satisfactory approximation both in terms of initial stiffness and peak load. The average error in terms of peak-strength is approximately 10% for both tests. Moreover, the model was able to properly simulate the two different non-linear experimentally observed behaviours.

More specifically, the numerical response is characterised by a hardening post-yielding behaviour, from 1% to 4% of drift for specimen SDCH-0850 and a more brittle behaviour, characterised by a sharp strength degradation after 3% drift for specimen SDCH-4150. In both cases, the numerical hysteretic loops, strongly characterised by unloading/reloading stiffness degradation and pinching effects, fit the experimental responses with a satisfactory approximation.

Figure 13 compares the experimental and numerical shear stress-strain responses of the joint panel for both tests The numerical response is plotted until 3% of beam drift is reached After this point, in the experimental tests spalling of the concrete cover started, making it difficult to measure the panel shear strains. A good agreement is reported for both tests both in terms of peak-stress and hysteretic loops. The numerical model was able to simulate with satisfactory approximation the reloading stiffness degradation and the strength degradation that characterises the response of specimen SCDH-J4150.
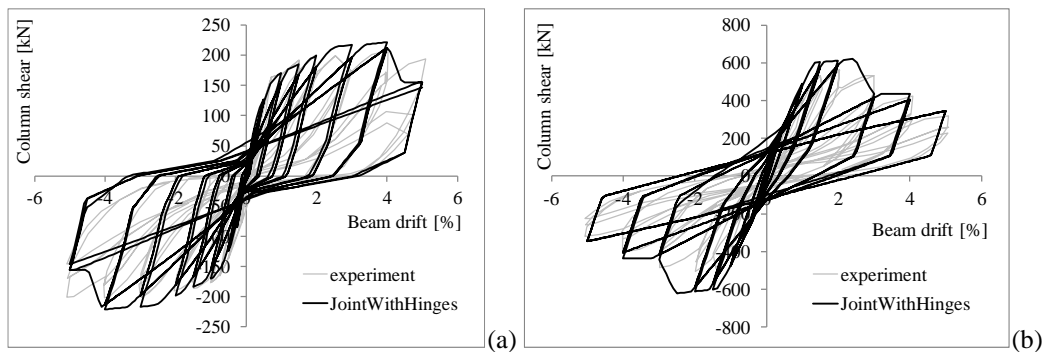

Figure 12   **Global response of (a) SCDH-0850 and (b) SCDH-4150 tests.**
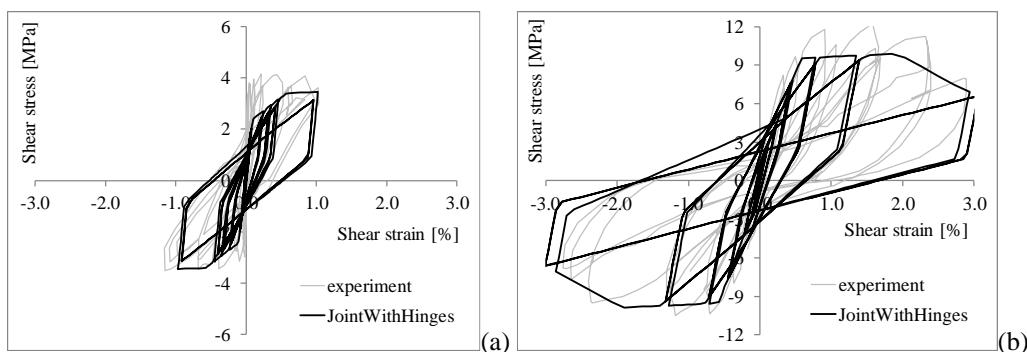

Figure 13   **Response of the joint panel relative to (a) SCDH-0850 and (b) SCDH-4150 tests.**

Finally, Figure 14 shows the moment-rotation responses of the right hinge. A strong non-linear response is observed in the case of specimen SCDH-0850 (Figure 14a) with ultimate rotation of 2.2% and pinching behaviour governed by the bond-slip mechanism of the beams' longitudinal bars. Conversely, in the case of specimen SCDH-4150 (Figure 14b) the interface behaviour is almost elastic. These figures clearly show the two different failures. In Specimen *SCDH-0850* (low beam reinforcement ratio) the beam section yields first, and the shear force transmitted to the joint panel causes damage but is too low to induce failure. Conversely, in specimen *SCDH-4150* (high beam reinforcement ratio) the beam remains basically elastic and transmits a higher shear force that induces panel failure.
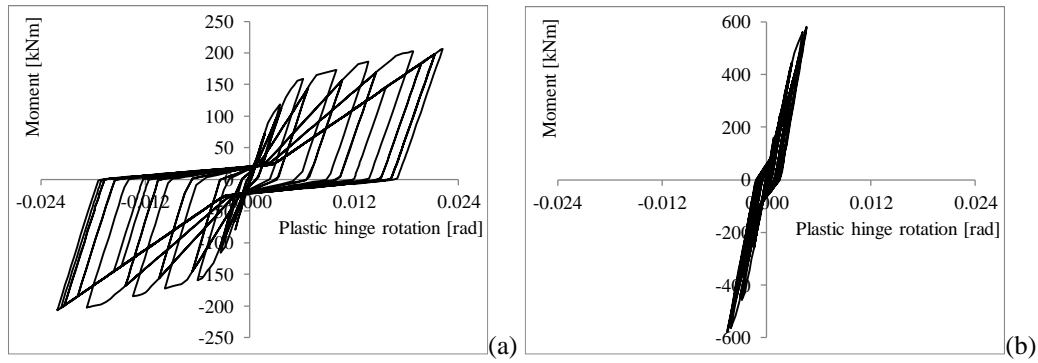
Figure 14   Right beam flexural responses of (a) SCDH-0850 and (b) SCDH-4150 tests.

Exterior Beam-Column Joint

The proposed *JointWithHinges* model is applied here to four full-scale exterior unreinforced beam-column sub-assemblages experimentally described in [De Risi et al. 2017]. The specimens are characterised by two different joint aspect ratios and beam longitudinal reinforcements. All tests were performed applying a cyclical displacement at the free beam end using the geometrical layout shown in Figure 15. The applied external force (F) corresponding to each drift ($\delta = \Delta / L_b$) was monitored during the test.

A constant axial load P=260 kN (or 15% of the concrete section ultimate compression) was applied at the column top. In all specimens the column had a 300x300mm cross section with 8ϕ20 longitudinal steel bars. Two beam cross sections were considered: 300x400mm for the #1bP and #2bP tests; 300x600mm for the #1cP and #2cP tests. For each beam cross section, two symmetric steel reinforcement layouts (strong and weak layout) were considered in order to investigate different failure mechanisms. More specifically, 4ϕ20 longitudinal bars (both top and bottom) were used in specimens #1bP and #1cP and 4ϕ16 in specimens #2bP and #2cP. The beam width (b_b), depth (h_b) and steel reinforcement (A_s), the concrete compression strength (f_c) and the steel yield stress (f_y) are reported in Table 4. The concrete peak and ultimate strains are assumed 0.2% and 2%, respectively, and the residual stress is 30% of the peak stress. No transversal steel reinforcement was considered in the joint panel while the beam and column stirrups were designed to avoid shear failure. The beam longitudinal bars were anchored within the joint by means of bent hooks with circular diameter 2.5 times the bar diameter (Figure 15).
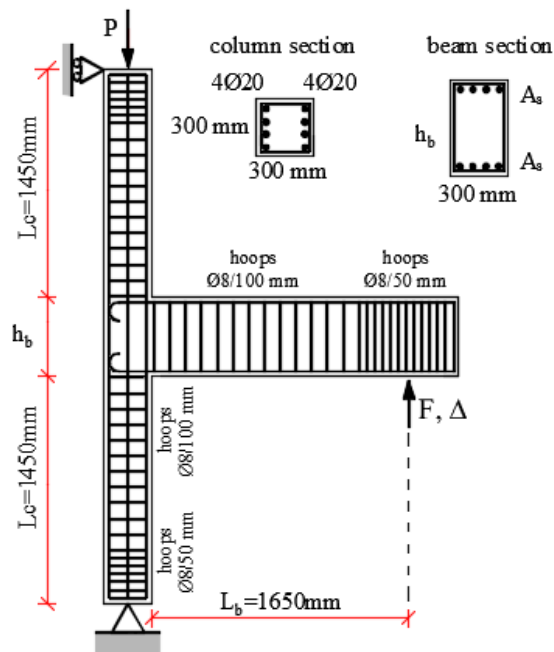

Figure 15 Exterior beam-column joint assemblage tested by [De Risi et al. 2017].

Table 4: Material parameters and steel reinforcement (equal top and bottom).

Test	b_b [mm]	h_b [mm]	A_s [-]	f_c [MPa]	f_y [MPa]
#1bP	300		4ϕ20		370
#2bP		400	4ϕ16	17.7	330
#1cP	300		4ϕ20		370
#2cP		600	4ϕ16	17.7	330

The tests with the lower aspect ratio (#1bP and #2bP) showed a joint shear failure at loads of 51.68kN and 50.27kN, respectively. The strain measures of the longitudinal steel bars confirmed no yielding. However, the maximum strains reached in specimen #2bP (0.16%) were very close to the nominal yield strain (0.17%) indicating that the beam steel ratio of this test can be considered as the transition between the joint-shear and the beam-yielding mechanisms. The diagonal cracks in the joint panel appear at 0.50% and 0.75% drift for specimens #1bP and #2bP, respectively. The peak load is reached in the drift range between 2.0% and 3.0%. After the peak, both tests showed a softening post-cracking branch with the progressive reduction of lateral stiffness. More specifically, in Test #1bP the load capacity dropped sharply due to concrete cover spalling after a 4.0% drift. Conversely, Test #2bP showed a uniform strength reduction with the drift increase. At the end of the test (6% drift), the residual strength was approximately 50% of the recorded peak load.

Figure 16 reports the numerical F-δ global responses while Figure 17 shows the joint panel shear stress-strain curves. A good agreement is generally observed between numerical and experimental responses. In all four cases the model is able to fit the pre- and post-peak experimental envelopes and hysteretic behaviours with a satisfactory approximation.

The largest differences are observed in the post-peak branches of the tests with higher reinforcement ratio (#1bP Test and #1cP Test). More specifically, the largest differences are recorded in the negative loading direction of the higher aspect-ratio (#1cP) test. In this case the specimen is characterised by a non-symmetric response while the numerical response is symmetric because of to the constitutive laws adopted. In the experiments the shear-strains were registered up to a 3.0% global drift for tests #1bP and #2bP, and up to a 2.0% drift for tests #1cP and #2cP. After these deformation levels, significant cracking made the strain readings difficult and unreliable.

Figure 17 compares the experimental and numerical joint panel shear responses up to the above-mentioned drift limits. The macro-model overestimates the plastic shear drifts, mostly in the last cycles. The average experimental ultimate shear drift is approximately 1.2% while the average numerical prediction is approximately 2.0%. This matching could be improved by using a more refined constitutive law (this enhancement is part of an ongoing study). Moreover, it is important to point out that the shear drifts predicted by the model represent both the diagonal shear cracking of the joint panel and the severe spalling of the perimeter concrete that was experimentally observed in the post-peak stage of the joint response.

Table 5 reports the comparison between experimental and numerical peak-values. The first three columns report the numerical peak shear force ($V_{b,num}$), the experimental value ($V_{b,exp}$) and the nominal yielding value ($V_{b,y}$). The macro-model, coherently with the experiment, does not predict beam yielding. The difference between the numerical and experimental prediction (V-err) reported in the second to the last column indicates the numerical response accuracy. The largest error is observed in test #2cP with a 15% error. However, even in this case the error can be considered acceptable for practical applications. In the central part of Table 5, the ratio between the maximum elongation of the steel fibres and the corresponding yield limit ($\rho\varepsilon_{num}$) is reported and compared with the corresponding ratio recorded during the tests ($\rho\varepsilon_{exp}$). The error falls in the 10-15% range and can again be considered compatible with standard engineering predictions.
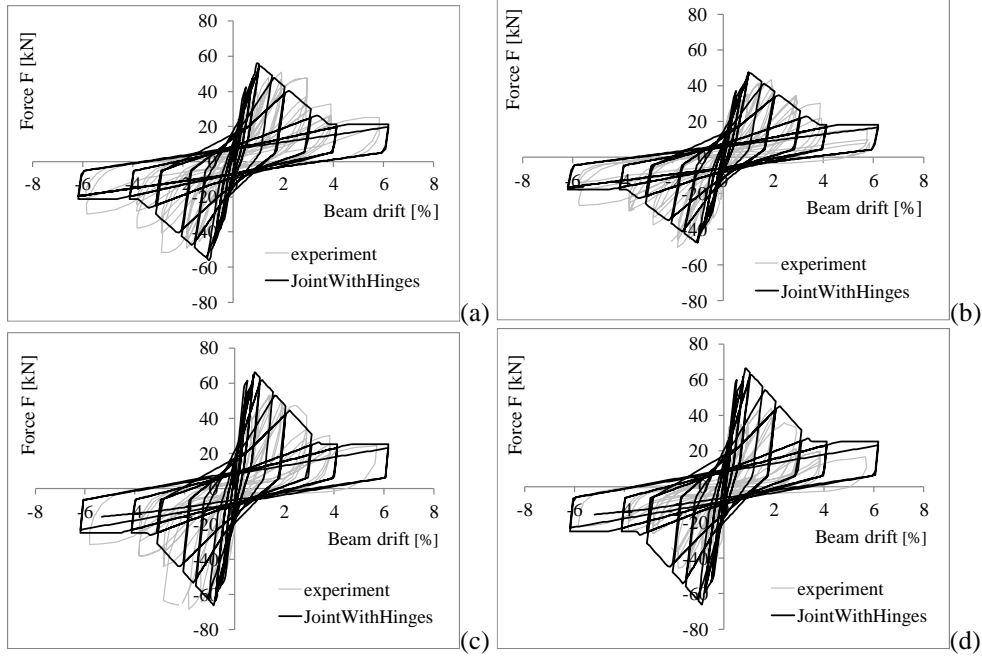
Figure 16   Global response of: (a) Test_1bP; (b) Test_2bP; (c) Test_1cP and (d) Test_2cP.
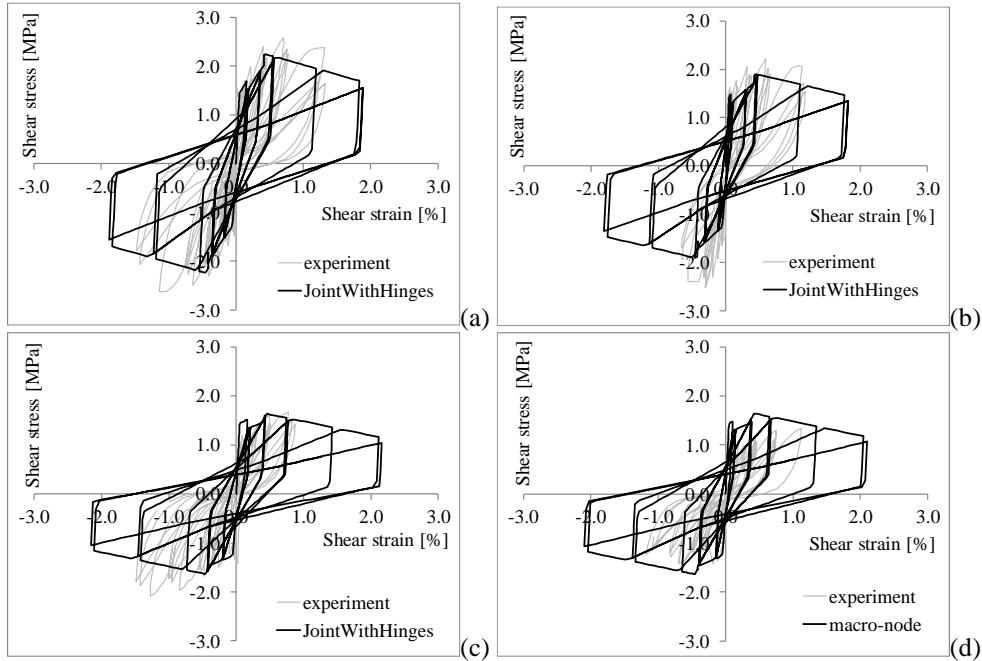

Figure 17   Joint panel shear response for: (a) Test_1bP; (b)Test_2bP; (c) Test_1cP and (d) Test_2cP.

Table 5: Peak response parameters

Test	$V_{b,num}$ [kN]	$V_{b,exp}$ [kN]	$V_{b,y}$ [kN]	$\rho\varepsilon_{num}$ [%]	$\rho\varepsilon_{exp}$ [%]	V-error [%]	ε–error [%]
#1bP	51.57	51.68	89.58	54.40	47.40	0.12	14.77
#2bP	47.70	47.00	52.50	80.20	91.17	1.33	12.03
#1cP	66.27	68.36	143.52	41.96	42.11	1.46	0.36
#2cP	60.00	46.90	83.56	71.87	64.71	15.68	11.06

CONCLUSIONS AND FUTURE DEVELOPMENTS

Recent seismic events have shown that the seismic behaviour of existing non-conforming RC buildings is strongly affected by the nonlinear response of the (often unreinforced) beam-column joints that can experience shear failure of the joint panel, bond-slip of the longitudinal steel bars or yielding and failure in the plastic hinge regions. Even though several numerical models have been proposed, the explicit modelling of the beam-column joint regions by means of simplified but sufficiently reliable models suitable for engineering practice still remains an open issue.

This paper presents a discrete *JointWithHinges* macro-element that accounts for the non-linear behaviour of the beam-to-column joints and of the connected plastic hinges. The model is based on a very simple mechanical scheme made of a quadrilateral (that represents the joint panel) whose rigid edges are connected to the connected beams and columns through non-linear finite-length hinges modelled following a fibre-section approach. In the present form, the model accounts for the cyclic response and diagonal shear failure of the joint panel, the nonlinear bending and linear shear deformations of the plastic hinge regions and the bond-slip of the beam bars. The main novelty lies in the fact that the non-linear behaviour of a plane frame can be modelled through the assemblage of non-linear *JointWithHinges* elements connected by means of elastic (or inelastic) beam or column elements.

Unlike other models, the proposed approach concentrates the main nonlinearities in the same macro-element. This allows *i*) a reliable modelling strategy that includes the non-linear coupling between the joint and the connected plastic hinge regions and *ii*) an enhancement in the model robustness and computational efficiency. In the current implementation the shear response of the plastic hinges is assumed linear elastic. The model is validated through the numerical simulations of the cyclical behaviour of experimentally tested internal and external joint assemblages with different geometries and steel-reinforcement ratios. The predictions obtained using the proposed model show its effectiveness in predicting both the cyclical behaviour and the failure mechanisms of the studied systems.

In the present study the authors concentrate on simple constitutive laws that represent the mechanics that govern the response of RC beam-column joints. This choice was driven by the fact that this study mainly focuses on the macro-model formulation and calibration strategy. Further developments should consider: *i*) enhancements to the non-linear modelling of the shear behaviour of the joint panel; *ii*) nonlinear shear-bending interaction in the plastic hinge regions; *iii*) explicit interaction between bar bond-slip and shear responses both in the joint panel and in the plastic hinges; *iv*) refinement of the steel constitutive law to include bar buckling; and *v*) extension to the three-dimensional case. Additional validation studies and entire frame analyses are also envisioned together with the development of an automated procedure for selecting the model mechanical parameters.

REFERENCES

Alire D.A. Seismic Evaluation of Existing Unconfined RC Beam-Column Joints, MSCE Thesis, Dept. of Civil Engineering, University of Washington, 2002.

Altoontash A. Simulation and damage models for performance assessment of RC beam–column joints. Ph.D. dissertation. Stanford (CA): Department of Civil and Environment Engineering. Stanford University, 2004.

Anderson M., Lehman D., Stanton J. A cyclic shear stress–strain model for joints without transverse reinforcement. Engineering Structures, 2008; 30(4):941-954.

Ates S., Kahya V., Yurdakul M., Adanur S. Damages on RC buildings due to consecutive earthquakes in Van. Soil Dynamics and Earthquake Engineering, 2013; 53:109-118.

Bakir P.G., Boduroğlu, H.M. A new design equation for predicting the joint shear strength of monotonically loaded exterior beam-column joints. Engineering Structures, 2002; 24(8):1105-1117.

Biddah A., Ghobarah A. Modelling of shear deformation and bond slip in RC joints. Struct. Eng Mech, 1999; 7(4):413–32.

Braga F., Gigliotti R., Laterza M., D'Amato M., Kunnath S. Modified Steel Bar Model Incorporating Bond-Slip for Seismic Assessment of Concrete Structures. J. Struct. Eng, 2012, 138:1342-1350.

Caliò I., Marletta M, Pantò B. A Simplified Model for the Evaluation of the Seismic Behaviour of Masonry Buildings, in B.H.V. Topping, (Editor), Proc. of the 10th Int. Civil-Comp, Stirlingshire, UK, 2005, Paper 195.

Caliò I., Marletta M., Pantò B., A new discrete element model for the evaluation of the seismic behaviour of unreinforced masonry buildings. Engineering Structures, 2012; 40:327-338.

Caliò I., Pantò B. A macro-element modelling approach of Infilled Frame Structures. Computers & Structures, 2014; 143:91-107.

Celik O.C. Observed Beam-Column Joint Failures During 17 August 1999 Kocaeli and 12 November 1999 Duzce, Turkey Earthquakes. The Paramount Role of Joints into the Reliable Response of Structures, 2000; pp. 197-206. Springer, Dordrecht.

Celik O.C., Ellingwood B.R. Modeling Beam-Column Joints in Fragility Assessment of Gravity Load Designed RC Frames. Journal of Earthquake Engineering, 2008; 12(3):357-381.

Coleman J, Spacone E. Localization Issues in Force-Based Frame Elements, ASCE Journal of Structural Engineering, 2001; 127(11): 1257-1265.

D'Amato M., Braga F., Gigliotti R., Kunnath S., Laterza M. Validation of a modified steel bar model incorporating bond-slip for seismic assessment of concrete structures. ASCE Journal of Structural Engineering, 2012; 138(11):1351-1360.

De Risi M.T., Ricci P., Verderame G.M., Manfredi G. Experimental assessment of unreinforced exterior beam–column joints with deformed bars. Engineering Structures, 2016; 112:215-232.

De Risi M.T., Verderame G.M. Experimental assessment and numerical modelling of exterior non-conforming beam-column joints with plain bars. Engineering Structures, 2017; 150:115-134.

Doğangün A. Performance of RC buildings during the May 1, 2003 Bingöl Earthquake in Turkey. Engineering Structures, 2004; 26(6):841-856.

Elmorsi M., Kianoush M.R,. Tso W.K. Modeling bond-slip deformations in RC beam–column joints. Canad J Civ Eng, 2000; 27:490–505.

EN, B. 1-1. Eurocode 2: Design of concrete structures–Part 1-1: General rules and rules for buildings. European Committee for Standardization (CEN), 2004.

Filippou F. C., Popov E. P., Bertero V. V. Modeling of R/C joints under cyclic excitations. Journal of Structural Engineering, 1983, 109(11), 2666-2684.

Ghosh S.K. Observations on the Performance of Structures in the Kobe Earthquake of January 17, 1995. PCI journal, 1995; 40(2):14-22.

Hwang S.J., Lee, H.J. Strength prediction for discontinuity regions by softened strut-and-tie model. Journal of Structural Engineering, 2002; 128(12):1519-1526.

Ibarra L.F., Krawinkler H. Global collapse of frame structures under seismic excitations, Appendix B, Pacific Earthquake Engineering Research Center Berkeley, CA, 2005.

Izzudin B.A., Karayannis C.G., Elnashai A.S. Advanced non-linear formulation for RC beam-columns, J. Struct. Eng. (ASCE), 1994; 120(10):2913-2934.

Jeon J.-S., Shafieezadeh A., DesRoches R. Statistical models for shear strength of RC beam-column joints 1 using machine-learning techniques. Earthquake Engineering and Structural Dynamics, 2014; 43(14):2075-2095.

ACI Committee 318, "Building Code Requirements for Structural Concrete (ACI 318-19) and Commentary (ACI 318R-19)," American Concrete Institute, Farmington Hills, MI, 2019, 623 pp.

Kent D.C., Park R. Flexural members with confined concrete. J. Struct. Div., ASCE, 1971; 97(7):1969-90.

Kim J., & LaFave J. M. Key influence parameters for the joint shear behaviour of reinforced concrete (RC) beam–column connections. Engineering structures, 2007, 29(10), 2523-2539.

Kim J., LaFave J. M., Song J. A new statistical approach for joint shear strength determination of RC beam-column connections subjected to lateral earthquake loading. Structural Engineering and Mechanics, 2007, 27(4), 439-456.

Kim J., LaFave J. M. Probabilistic joint shear strength models for design of RC beam-column connections, 2008, ACI Structural Journal, 105(6), 770.

Kunnath S.K., Hoffmann G., Reinhorn A.M., Mander J.B. Gravity load-designed RC buildings—part II: evaluation of detailing enhancements. ACI Struct J, 1995; 92(4):470–478.

Lehman D., Stanton J., Anderson M., Alire D., Walker S. Seismic performance of older beam-column joints. 13th World Conference On Earthquake Engineering, August 2004.

Lima C., Martinelli E., Macorini L., Izzuddin B.A. Modelling beam-to-column joints in seismic analysis of RC frames. Earthquakes Struct., 2017; 12 (1):119-133.

Lowes L., Mitra N., Altoontash A. A Beam-Column Joint Model for Simulating the Earthquake Response of RC Frames. PEER 2003/10, February 2004.

Lowes L.N., Altoontash A. Modeling reinforced-concrete beam-column joints subjected to cyclic loading. Journal of Structural Engineering, 2003; 129:1686-1697.

Marini A., Spacone E. Analysis of R/C Elements Including Shear Effects. ACI Structural J., 2006; 103(5):645-655.

Masi A., Chiauzzi L., Santarsiero G., Manfredi V., Biondi S., Spacone E., Del Gaudio C., Ricci P., Manfredi G., Verderame G.M. Seismic response of RC buildings during the Mw 6.0 August 24, 2016 Central Italy earthquake: the Amatrice case study. Bulletin of Earthquake Engineering, 2017; doi:10.1007/s10518-017-0277-5.

McKenna F., Fenves G.L., Scott M.H. OpenSees: Open System for Earthquake Engineering Simulation‖. 44 Pacific Earthquake Engineering Research Center. University of California, Berkeley, CA, USA. 45, 2010

Melo J., Varum H., Rossetto T. Cyclic behaviour of interior beam–column joints reinforced with plain bars. Earthquake Engineering & Structural Dynamics, 2015; 44(9):1351-1371.

Metelli G., Messali F., Beschi C., Riva P. A model for beam–column corner joints of existing RC frame subjected to cyclic loading. Engineering Structures, 2015; 89:79-92.

Mitra N., Lowes L.N. Evaluation and advancement of a RC beam-column joint model. Proc., 13th. World Conference on Earthquake Engineering, Vancouver, B.C., Canada, 2004.

Mitra N., Lowes L.N. Evaluation, Calibration, and Verification of a RC Beam–Column Joint Model. Journal of Structural Engineering, 2007; 133(1):105-120.

Mulas M.G. A structural model for panel zones in non linear seismic analysis of steel moment-resisting frames. Engineering structures, 2004; 26(3):363-380.

NTC 2018, Italian Ministry of Infrastructure, D.M. 2018. Aggiornamento delle «Norme tecniche per le costruzioni, GU Serie Generale n.42 del 20-02-2018 - Suppl. Ord. n. 8.

Otani S. Inelastic analysis of R/C frame structures. Journal of the Structural Division, 100 (Proc. Paper 10686), 1974.

Pampanin S., Magenes G., Carr A. Modelling of shear hinge mechanism in poorly detailed RC beam–column joints. Proceedings of the FIB 2003 symposium, 2003.

Pantelides C. P., Hansen J., Ameli M. J., & Reaveley L. D. Seismic performance of reinforced concrete building exterior joints with substandard details. Journal of Structural Integrity and Maintenance, 2017, 2(1), 1-11.

Pantò B., Caliò I., Lourenço P.B. A 3D discrete macro-element for modelling the out-of-plane behaviour of infilled frame structures. Engineering Structures, 2018; 175:371-385.

Pantò B., Cannizzaro F., Caliò I., Lourenço, P.B. Numerical and experimental validation of a 3D macro-model for the in-plane and out-of-plane behavior of unreinforced masonry walls. International Journal of Architectural Heritage, 2017; 11(7):946-964.

Pantò B., Rapicavoli D., Caddemi S., Caliò I. A Fibre Smart Displacement Based (FSDB) beam element for the nonlinear analysis of RC members. International Journal of Non-Linear Mechanics, 2019; 117,103222.

Park S., Mosalam K.M. Simulation of RC Frames with Nonductile Beam-Column Joints. Earthquake Spectra, 2013; 29(1):233-257.

Paulay T., Park R., Priestley M.J.N. RC Reinforced concrete beam-column joints under seismic actions, ACI Journal, 1978; 75(11):585-593.

Paulay T., Priestley M.J.N. Seismic design of RC and masonry buildings. New York: John Wiley Publications, 1992.

Parate K., Kumar R. Shear strength criteria for design of RC beam–column joints in building codes. Bulletin of Earthquake Engineering, 2019, 17(3), 1407-1493.

Ricci P., De Luca F., Verderame G.M. 6th April 2009 L'Aquila earthquake, Italy: RC building performance. Bulletin of Earthquake Engineering, 2011; 9(1):285-305.

S. Park, K.M. Mosalam Analytical Model for Predicting Shear Strength of Unreinforced Exterior Beam-Column Joints. Aci Structural Journal, 2012; 109 (2):149-160.

Scott M.H., Fenves, G.L. Plastic hinge integration methods for force-based beam–column elements. Journal of Structural Engineering, 2006; 132(2):244-252.

Scott R.H., Feltham I., Whittle, R.T. RC beam-column connections and BS 8110. Structural Eng., 1994; 72(4):55-60.

Sezen H., Whittaker A.S., Elwood K.J., Mosalam K.M. Performance of RC buildings during the August 17, 1999 Kocaeli, Turkey earthquake, and seismic design and construction practise in Turkey. Engineering Structures, 2003; 25(1):103-114.

Sharma A., Eligehausen R., Reddy G. R. A new model to simulate joint shear behavior of poorly detailed beam–column connections in RC structures under seismic loads, Part I: Exterior joints. Engineering Structures, 2011; 33(3):1034-105.

Shin M., LaFave J. M. Modeling of cyclic joint shear deformation contributions in RC beam-column connections to overall frame behaviour, 2004; Structural Engineering and Mechanics, 18(5): 645-670.

Spacone E., Ciampi V., Filippou F.C. Mixed formulation of non-linear beam finite element. Comput. Struct., 1996; 58(1):71-83.

Vecchio F.J., Collins M.P. The modified-compression field theory for RC elements subjected to shear. J Amer Concr Inst, 1986; 83(2):219–31.

Viawanthanatepa S., Popov E.P., Bertero V.V. Effects of Generalized Loadings on Bond of Reinforcing Bars Embedded in Confined Concrete Blocks. Report UCB/EERC-79 / 22. Berkeley: EERC, Univ. of California, 1979.

Vollum R., Parker, D. External beam–column joints: design to Eurocode 2. Magazine of Concrete Research, 2008; 60(7):511-521.

Vollum R.L.,Newman J.B. The design of external, RC beam-column joints. Struct. Engineer, 1999; 77(23-24):21-27.

Walker S. Seismic performance of existing reinforced concrete beam–column joints. MSCE, MSCE Thesis, Dept. of Civil Engineering, University of Washington, 2001, 308 p.

Youssef M., Ghobarah A. Modelling of RC Beam-Column Joints and Structural Walls. Journal of Earthquake Engineering, 2001; 5 (1):93-111.

Zhao W., Yang H., Chen J., Sun, P. A proposed model for nonlinear analysis of RC beam-column joints under seismic loading. Engineering Structures, 2019; 180: 829-843.